

RSC Advances



This is an *Accepted Manuscript*, which has been through the Royal Society of Chemistry peer review process and has been accepted for publication.

Accepted Manuscripts are published online shortly after acceptance, before technical editing, formatting and proof reading. Using this free service, authors can make their results available to the community, in citable form, before we publish the edited article. This *Accepted Manuscript* will be replaced by the edited, formatted and paginated article as soon as this is available.

You can find more information about *Accepted Manuscripts* in the [Information for Authors](#).

Please note that technical editing may introduce minor changes to the text and/or graphics, which may alter content. The journal's standard [Terms & Conditions](#) and the [Ethical guidelines](#) still apply. In no event shall the Royal Society of Chemistry be held responsible for any errors or omissions in this *Accepted Manuscript* or any consequences arising from the use of any information it contains.

Theoretical challenges in understanding the inhibition mechanism of copper corrosion in acid media in the presence of three triazole derivatives

Lei Guo,^a Weipeng Dong,^b Shengtao Zhang^{*a}

Abstract Using quantum chemical and molecular dynamics approaches, we investigated the corrosion inhibition mechanism of Cu/HNO₃ system in the presence of three triazole derivatives. The interactions between inhibitors and copper substrates were described by the periodic slab model using density functional theory calculations. Dispersion forces are taken into account in the OBS (Ortmann, Bechstedt, and Schmidt) framework correcting both energies and gradients. It was found that the perpendicular configuration is energetically more stable than the parallel configuration for all the three inhibitors. Diffusion model was also employed to compare the protective effect of the inhibitor membranes. A good correlation was observed between the related parameters and inhibition efficiency data reported in the literature.

Key Words Copper corrosion, Triazoles inhibitors, Molecular dynamics, Quantum chemical

1. Introduction

Copper metal is widely used in microelectronic packaging. The advantages of copper over aluminium are lower resistance and higher reliability. But copper is an active metal, which readily undergoes corrosion in acid medium. Corrosion is a destructive phenomenon by which the metallic structures are destroyed gradually through chemical or electrochemical reactions. Therefore, various attempts must be employed to prevent or retard these undesired reactions. The application of inhibitors, *viz.* specific organic compounds containing heteroatoms, aromatic rings or π electrons, is one of the most practical methods to combat corrosion.¹⁻³

Nowadays, N- and S-containing triazole derivatives have attracted more attention for their excellent corrosion inhibition performance.⁴⁻⁷ Zarrouk *et al.*⁸⁻¹⁰ have recently reported considerable inhibition efficiencies of such three compounds, that is, 3-amino-1,2,4-triazole (ATA), 3,5-diamino-1,2,4-triazole (DAT), and (4-amino-3-hydrazino-5-mercapto-1,2,4-triazole) AHMT (see Table 1), for copper corrosion in 2 M HNO₃ medium. The results of their electrochemical and weight loss measurements showed that all three compounds reduce the corrosion rate of copper substantially in HNO₃ medium. At any given inhibitor concentration, the corrosion rate follows the order: $v(\text{AHMT}) < v(\text{DAT}) < v(\text{ATA})$, which indicates that AHMT exhibits the best inhibitive performance among these additives. A recondite explanation was suggested that the inhibitor molecules hinder the dissolution of copper by forming a protective hydrophobic film on the surface.

Although their experimental work has shown that the inhibitor molecules act by adsorption at the metal

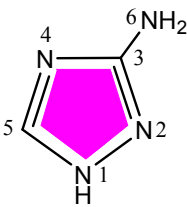
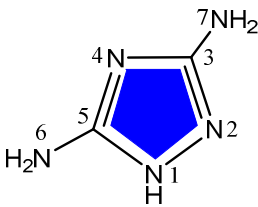
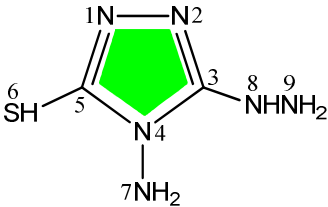
^aSchool of Chemistry and Chemical Engineering (Chongqing University), Chongqing 400044, China. E-mail: stzhcq@163.com; Fax:+86 023 65106756.

^bQuality Education Center (Xinxiang University), Xinxiang 453003, China

interface, the protection mechanism of organic corrosion inhibitors has not been clearly understood. Actually, little attention has been paid to how these organic surface modifiers bind to metal surfaces, and why seemingly minor modifications in the structures of organic active compounds can have a profound effect on their efficacy. The advancements in computer simulation techniques hold promise that questions regarding the inhibitive properties of such compounds can be addressed at the atomic level. Therefore, there is a wealth of theoretical studies concerning the associations between molecular mechanism and inhibition effect.¹¹⁻¹⁵

In this work, prompted by the successful application of theoretical calculations in corrosion inhibitor research, an attempt is devoted to elucidate the inhibition mechanism of ATA, DAT and AHMT compounds and to give a suitable explanation to the experimental results by using quantum mechanics and molecular dynamics methods, which have proven to be very suitable methods for gaining new physical insight into the actual inhibition mechanism.

Table 1 Percent inhibition efficiency, *IE* (%), of three triazole derivatives as corrosion inhibitors of copper in nitric acid solution (0.01 M, 303 K)^a

		
3-amino-1,2,4-triazole	3,5-diamino-1,2,4-triazole	4-amino-3-hydrazino-5-mercapto-1,2,4-triazole
ATA	DAT	AHMT
82.2	86.5	91.7

^a Taken from Refs. ⁸⁻¹⁰, obtained through weight loss experiments.

2. Methods and definitions

2.1 Computational details

The geometry pre-optimizations of the molecules studied have been carried out by applying the molecular-mechanics method. Thereafter, the optimized equilibrium structures of molecules have been calculated by DFT methods, B3LYP and PW91 functionals, using 6-311++G** basis set, which are embodied in Gaussian 03 program package.¹⁶ Frequency calculation was executed simultaneously, and no imaginary frequency was found, confirming the minimum-energy structures. The global and local indexes of reactivity were calculated with Koopmans approximation.¹⁷

A prediction of copper crystal morphology was necessary before the simulation process. Three representative algorithms, *i.e.*, the Bravais–Friedel–Donnay–Harker (BFDH) method, the surface free-energy (SFE) model, and the attachment energy (AE) method, were utilized to predict crystal structures. More detailed descriptions about

these models can be found in Ref.¹⁸ and the references therein.

The interactions between interested inhibitors and the Cu(111) surface was carried out in a simulation box with periodic boundary conditions using the DMol³ program.¹⁹ The Cu(111) surface was modelled with a four-layer slab model. In this model, there were 25 copper atoms in each layer representing a (5 × 5) unit cell, and a 20 Å vacuum region between two adjacent layers to ensure the repeated slabs decoupled. The generalized gradient approximation (GGA) functional developed by Perdew and Wang (PW91)^{20, 21} has been employed in conjunction with a double numeric quality basis set with polarization functions (DNP), where the reliability of this level of theory in studying the metal surface has been confirmed.²²⁻²⁴ The electron-ion interaction was described by density functional semi-core pseudopotentials for metals, which are intended for use with density functional local orbital methods. A Monkhorst-Pack grid of 6 × 6 × 1 was used to sample the Brillouin zone. The tolerances of energy, gradient, and displacement convergence were 1×10^{-5} Ha, 2×10^{-3} Ha Å⁻¹, and 5×10^{-3} Å, respectively. A Fermi smearing of 0.001 Ha and a real space cutoff of 4.4 Å were used to improve computational performance. To explore the influence of van der Waals (vdW) forces on the adsorption geometry, the calculations were also performed by the PW91-D scheme, which includes a semiempirical dispersion correction of OBS²⁵ (Ortmann, Bechstedt, and Schmidt) that consists of employing a damped C_6R^{-6} energy term applied on top of the PW91 functional. We used a damping constant ($\lambda = 3.0 \times 10^{-5}$), in order to confirm the universality and transferability of this parameter, some solids and molecular systems (including Fe, Ar₂, benzene dimer, *etc.*) were studied (see Table S in the supporting information). For the PW91-D set of calculations, the Cu bulk lattice parameter has been recalculated with the PW91-D functional, which gives a slightly smaller value of 3.645 Å compared to the PW91 value of 3.650 Å.

After above calculations, the possible bonding modes between Cu atoms and the inhibitors were straightforward. Thus, all the most probable Cu-inhibitor (using a single Cu atom for simplicity) geometries have been fully optimized at the B3LYP/6-311++G** level using Gaussian 03. To better clarify the nature of the intermolecular contact, the QTAIM (quantum theory of atoms in molecules)²⁶ analysis was performed with the help of Multiwfn software²⁷ on the basis of the optimized structures.

Finally, diffusion model was selected to compare the protective effect of the inhibitor membranes. As shown in Fig. 1, the model consists of three regions, the substrate, middle layer and top layer. The substrate is Cu(111) surface. It contains five layers of copper atoms consisted of 405 frozen copper atoms. The middle layer contains an amorphous system of inhibitor membranes (composed of 50 inhibitors) and three H₃O⁺ corrosive particles. The top layer is a 30 Å vacuum slab. To obtain the equilibrium density of inhibitor membrane, molecular dynamics

(MD) simulations were carried out under NPT ensemble. The pressure was 1×10^{-4} GPa controlled by means of Berendsen Barostat method.²⁸ The temperature and simulation time are set to 303 K and 300 ps, respectively. Then, the middle layer was rebuilt with the calculated density by the Amorphous Cell module. After a molecular mechanics optimization, three diffusion models were submitted to a 1 ns MD run under the NVT ensemble. All the MD simulations were performed under COMPASS²⁹ force field, which was parameterized to predict various properties (molecular structures, vibrational frequencies, conformation energies, *etc.*) for molecules in isolation and in condensed phases (equations of state, cohesive energy density, *etc.*).

In all our simulations, we have neglected charge and solvent effects and performed the calculations at the neutral forms of the molecules. Although this is clearly an oversimplification of the factual situation, it is adequate to qualitatively illustrate the differences in the adsorption behaviour of three molecules and provide sufficient insight to rationalize previous experimental findings.

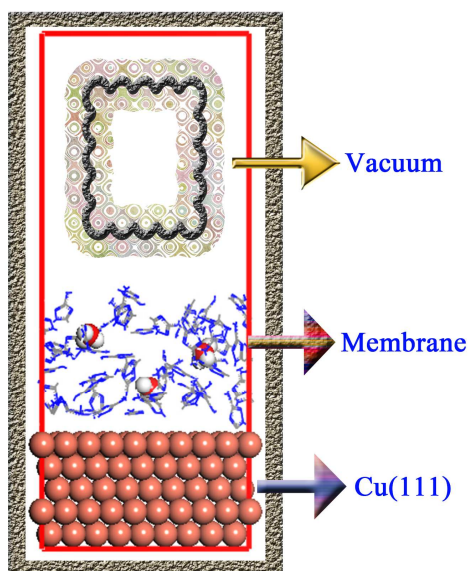


Fig. 1 Schematic of interface supercell (the design in the vacuum region is just for aesthetics).

2.2 Definitions of global reactivity descriptors

Within the conceptual framework of DFT, the chemical potential σ , which measures the escape tendency of an electron from equilibrium, is defined as:

$$\sigma = \left(\frac{\partial E}{\partial N} \right)_{v(r)} = -\chi \quad (1)$$

where σ is the first derivative of the total energy E relative to the electron number N , v is the external potential exerted by the nucleus and χ is the electronegativity.

The global hardness η can be seen as the resistance to charge transfer and is defined as:

$$\eta = 1/2 \left(\frac{\partial^2 E}{\partial N^2} \right)_{v(r)} \quad (2)$$

Using a finite difference approximation and Koopmans's theorem, the above expressions can be written as:

$$\sigma \approx (I + A)/2 \approx (E_{\text{HOMO}} + E_{\text{LUMO}})/2 = -\chi \quad (3)$$

$$\eta \approx (I - A)/2 = (E_{\text{LUMO}} - E_{\text{HOMO}})/2 \quad (4)$$

where E_{HOMO} and E_{LUMO} represent the energies of the highest occupied and the lowest unoccupied molecular orbitals (HOMO and LUMO), respectively, I is the ionization potential and A is the electron affinity. When two systems, Cu and inhibitor, are brought together, electrons will flow from (to) inhibitor to (from) Cu, until the chemical potentials become equal. As a first approximation, the fraction of transferred electrons (ΔN) was calculated according to Pearson theory³⁰ as follows:

$$\Delta N = \frac{\chi_{\text{metal}} - \chi_{\text{inh}}}{2(\eta_{\text{metal}} + \eta_{\text{inh}})} = \frac{\Phi - \chi_{\text{inh}}}{2\eta_{\text{inh}}} \quad (5)$$

where work function (Φ) is used for the electronegativity of metal surface, and the global hardness is neglected by assuming that for a metallic bulk $I = A$ because they are softer than the neutral metallic atoms³¹.

3. Results and discussion

3.1 Molecular reactivity

Quantum chemical calculations were performed to investigate the inhibition efficiencies of mentioned inhibitors. Table 2 shows the calculated theoretical parameters such as total energy, E_{HOMO} , E_{LUMO} , and ΔE , which provide information about the reactive behavior. In some ways, though, different calculation methods produced some changes in the electronic structure of the inhibitor molecules, but they follow the same trend for the presented properties of three molecules. However, the hybrid B3LYP functional is the most popular and reasonably accurate functional for the description of organic molecules. Thus, in subsection 3.1, unless explicitly attributed to PW91, the results refer to B3LYP/6-311++G** approach.

Table 2 Calculated quantum chemical properties for triazole derivatives ATA, BAT and AHMT

Molecule		E_{HOMO} (eV)	E_{LUMO} (eV)	ΔE (eV)	μ (Debye)	$\langle \alpha \rangle$ (\AA^3)	χ	η	ΔN
ATA	B3LYP	-6.26	-0.38	5.88	2.06	7.63	3.32	2.94	0.24
	PW91	-5.33	-0.98	4.34	1.95	8.02	3.15	2.17	0.37
DAT	B3LYP	-5.81	-0.65	5.16	2.60	9.15	3.23	2.58	0.29
	PW91	-4.86	-1.11	3.75	2.51	9.66	2.98	1.87	0.47
AHMT	B3LYP	-6.42	-1.06	5.37	4.99	13.62	3.74	2.68	0.19
	PW91	-5.53	-1.66	3.87	4.93	14.41	3.59	1.93	0.30

The electric dipole polarizability is a measure of the linear response of the electron density in the presence of an infinitesimal electric field, F , and represents a second-order variation in the energy, *viz.*³²:

$$\alpha_{a,b} = - \left\{ \frac{\partial^2 E}{\partial F_a \partial F_b} \right\} \quad a, b = x, y, z \quad (6)$$

The mean polarizability $\langle \alpha \rangle$ is a property observed when a molecule presents all orientations to the applied field and is evaluated by $\langle \alpha \rangle = (\alpha_{xx} + \alpha_{yy} + \alpha_{zz})/3$. As seen in Table 2, the polarizability values of ATA, DAT, and AHMT calculated with B3LYP are 7.63, 9.15, and 13.62 Å³, respectively. It means that the higher values of α facilitate the strong adsorption process, resulting in an increase in the inhibition efficiency.

The interaction between the inhibitor and the metal can be understood in the light of the frontier molecular orbital theory. In general, high lying HOMO favors the donation of molecular charge to metal, whereas low lying LUMO induces a back-donation of charge from metal to the molecule.^{33, 34} Both effects contribute to the enhanced molecule–metal interaction. It is understandable that the less negative HOMO and the smaller energy gap reflects a stronger chemisorbed bond and greater inhibitor efficiency. We regrettably find out that there is no direct correlation between E_{HOMO} , ΔE and inhibition efficiency determined experimentally. Consequently, this make the related descriptors (including χ , η and ΔN) invalid. Similar cases have been reported elsewhere.^{35, 36} It demonstrates that some molecular electronic properties cannot be used in a blind fashion to judge the inhibition effectiveness.

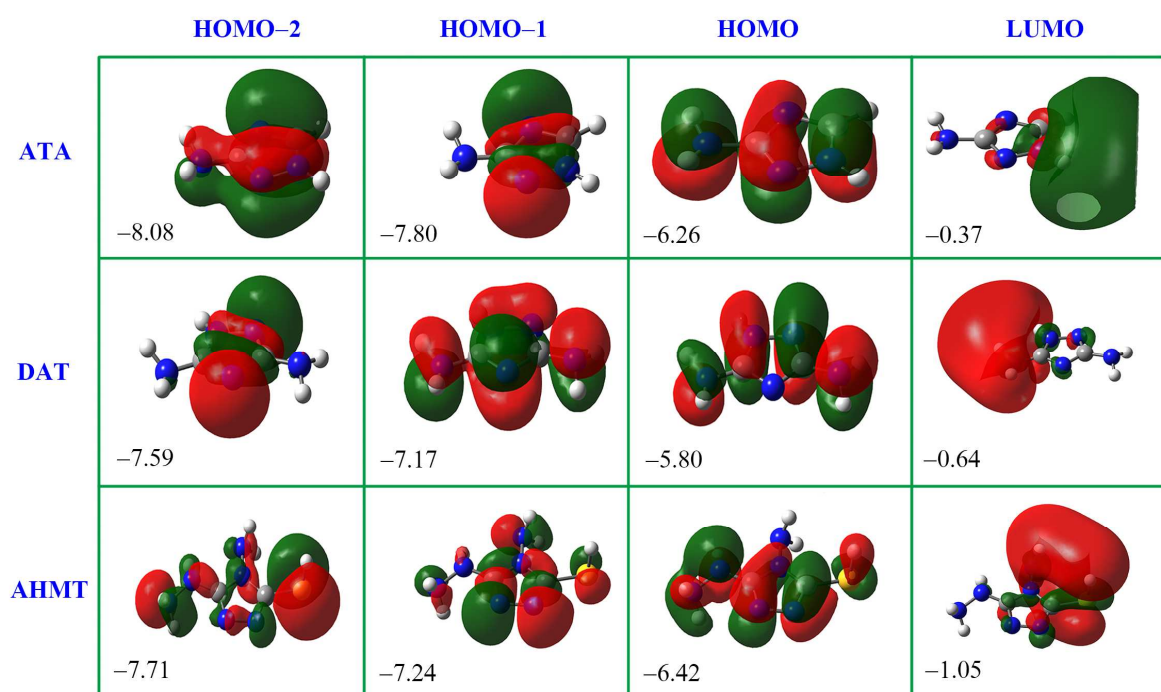


Fig. 2 Isosurface plots of HOMO– n ($n = 0, 1, \text{ and } 2$) and LUMO molecular orbitals for the molecules studied. The number below each molecular orbital plot is the energy (in eV) of the orbital.

Actually, the chemisorption through the nitrogen lone-pair electrons is very common for nitrogen-containing aromatic rings; Moreover, in the previous DFT study it has been shown that several high-lying orbitals mix with metal states, yet the interaction is mainly due to σ -type molecular orbitals.^{37, 38} The high-lying molecular orbitals (including HOMO– n and LUMO) are plotted in Fig. 2 for three azole derivatives. For all the molecules, the HOMO is a π -type orbital and is spread throughout the whole molecular skeleton. On the other hand, if the energy of the σ orbital was decisive for the inhibitor properties, the ranking of the compounds should be: $E_{\text{HOMO-1}}$ (AHMT) $>$ $E_{\text{HOMO-2}}$ (DAT) $>$ $E_{\text{HOMO-1}}$ (ATA). This agrees well with the experimental observations.

Dipole moment (μ) is another often used parameter in the corrosion inhibition studies.³⁹ There is no consensus on the influence of the dipole moment on corrosion inhibition. Some authors think that an increase of the dipole moment leads to decrease of inhibition, suggesting that a lower value of dipole moment will favour accumulation of the inhibitor in the surface layer.^{40, 41} Others argue that the increase of the dipole moment can lead to increase of inhibition, which could be related to the dipole–dipole interaction of molecules and metal surface.^{42, 43} Kocalj does not see this as a conflict and he demonstrates that the role of the molecular dipole depends on its orientation.³⁵ The dipole is almost parallel to the molecular plain for DAT (see Fig. 3a), whereas for ATA/AHMT the dipole points outward slightly. The higher value of μ obtained for AHMT is coherent with the second explanation indicating stronger dipole–dipole interactions of AHMT molecules and metallic surface in comparison to that of ATA/DAT.

The local reactivity has been analyzed by means of Fukui function, which are an indication of the reactive centers within the molecules. In the finite difference approximation, the condensed Fukui functions at the atom k can be calculated unambiguously for two situations⁴⁴:

$$f^+ = q(N) - q(N+1) \quad (\text{for nucleophilic attack}) \quad (7)$$

$$f^- = q(N-1) - q(N) \quad (\text{for electrophilic attack}) \quad (8)$$

Herein, $q(N+1)$, $q(N)$ and $q(N-1)$ are the charges at atom k of the anionic, neutral and cationic species, respectively. The definition of the dual descriptor Δf has close relationship with Fukui function⁴⁵:

$$\Delta f = f^+ - f^- \quad (9)$$

Unlike Fukui function, *via* Δf both types of reactive sites can be revealed simultaneously. If $\Delta f > 0$, then the site is favorable for a nucleophilic attack, whereas if $\Delta f < 0$, then the site is favorable for an electrophilic attack.

Table 3 Calculated Hirshfeld atomic charges and condensed Fukui functions for ATA, BAT and AHMT (numbers of atoms were shown in Table 1)

#	ATA				DAT				#	AHMT			
	q	f^+	f^-	Δf	q	f^+	f^-	Δf		q	f^+	f^-	Δf
N1	-0.01	0.02	0.10	-0.07	-0.04	0.02	0.09	-0.07	N1	-0.16	0.03	0.10	-0.06
N2	-0.20	0.03	0.16	-0.14	-0.22	0.03	0.19	-0.16	N2	-0.20	0.03	0.13	-0.10
C3	0.10	0.03	0.08	-0.06	0.10	0.02	0.08	-0.06	C3	0.11	0.02	0.06	-0.04
N4	-0.23	0.03	0.08	-0.05	-0.25	0.02	0.06	-0.04	N4	0.01	0.00	0.02	-0.02
C5	0.05	0.06	0.10	-0.05	0.12	0.02	0.07	-0.04	C5	0.03	0.01	0.09	-0.07
N6	-0.17	0.03	0.21	-0.18	-0.16	0.04	0.10	-0.06	S6	-0.02	0.16	0.13	0.02
N7					-0.17	0.02	0.15	-0.13	N7	-0.12	0.04	0.02	0.02
									N8	-0.08	0.01	0.14	-0.13
									N9	-0.16	0.02	0.07	-0.05

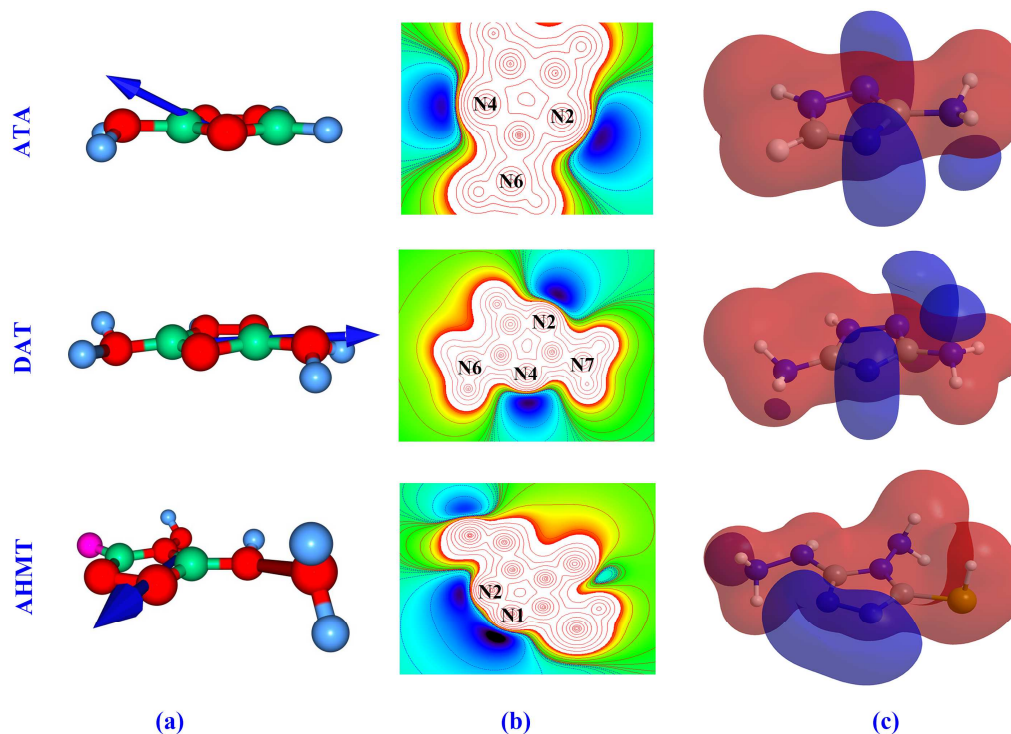
**Fig. 3** (a) Molecular dipoles shown as the arrows pointing from the barycenter of the molecules. (b and c) Contour and isosurface representation of electrostatic potential, respectively. Negative (positive) regions are colored blue (red).

Table 3 shows the atomic charges and condensed Fukui functions for the three inhibitors, which were easily evaluated from the Hirshfeld population analysis.⁴⁶ By examination of the f^+ values, it is evident that the preferred sites for nucleophilic attack in ATA, DAT and AHMT are near C5, N6 and S6 atoms, respectively. As for f^- , the N atoms of amino group are substantially charged, but they are passivated with H atom. So we thought that their reaction activities were reduced to some extent in neutral/vacuum condition. Moreover, the f^- values for N2 atoms

were relatively larger for all three molecules, which implied that these atoms preferred to provide electrons to form coordinate bonds with the metal atoms, so they were the electrophilic reactive sites during absorption. These results are basically consistent with previous HOMO/LUMO analysis. Besides, the adsorption geometries of the inhibitors can be anticipated from the electrostatic potential plots presented in Fig. 3b–c. These negative regions would be preferred sites for adsorption to metal surfaces. On this basis, it can be anticipated that ATA/DAT would adsorb through either N2 or N4 atoms, whereas AHMT would adsorb *via* N1 and N2 atoms.

3.2 Copper surfaces survey

We calculated the surface energy (E_{surf}) in a slab model as ⁴⁷

$$E_{\text{surf}} = \frac{E_{\text{slab}} - (N_{\text{slab}}/N_{\text{bulk}})E_{\text{bulk}}}{2A} \quad (10)$$

where E_{slab} and E_{bulk} are the total energies of the surface slab and the bulk unit cell, respectively. N_{slab} and N_{bulk} are the number of atoms contained in the slab and the bulk unit cells, respectively, and 'A' is the area of the surface unit cell. For each slab model, the work function (Φ) is obtained as follows ⁴⁸:

$$\Phi = E^{\text{vac}} - E_{\text{F}} \quad (11)$$

where E^{vac} is the vacuum local potential energy and E_{F} is the Fermi level.

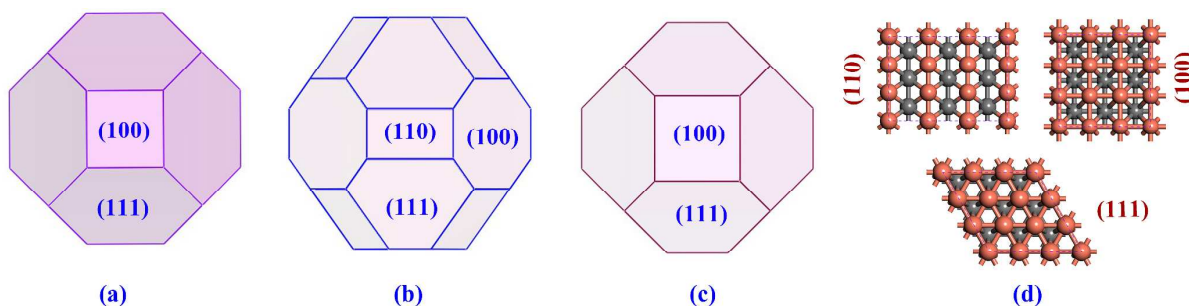


Fig. 4 (a, b, and c) The crystal habits of copper simulated by BFDH, SFE, and AE algorithms, respectively. (d) Upper views of the Cu (3×3) surface models.

The calculated surface energies, work functions, as well as the morphology results for copper crystal are listed in Table 4. Our results are in reasonable agreement with the available literature data.⁴⁹⁻⁵¹ After careful analysis of the simulated crystal morphology for copper, one will notice that the (111) face accounts for at least 42.0% of the crystal surface, and the most 77.6% in the BFDH model. The calculated surface energies decrease in the following sequence: (110) > (100) > (111). Additionally, a more intuitive micromorphology comparison diagram is produced, as shown in Fig. 4. Based on Fig. 4d, the regular (110), (100), and (111) surfaces have one type of surface atom with coordination numbers 7, 8, and 9, respectively. The calculated surface work functions

were found to be strongly dependent on the surface atom coordination number, and follow the expected trend (111) > (100) > (110), which means that the lower the coordination number of the surface atom the lower the work function value.⁵² Consequently, the densely packed Cu(111) surface model was chosen as representative to address the inhibitor adsorption-study because it is the most stable low Miller index copper surface and then the most abundant. In addition, the Cu(111) surface symmetry provides an advantage to systematically explore the potential energy surface of the adsorption system.

Table 4 Surface atom coordination number (N , #), surface energy, work function and morphology results for the clean copper surfaces studied here

hkl	Multiplicity ^a			% Total facet area			Surface energy (J m ⁻²)		Work function (eV)			N
	BFDH	SFE	AE	BFDH	SFE	AE	this work	calc. ^{49,50}	this work	calc. ⁵⁰	expt. ⁵¹	
(110)	12	12	12	/	26.5	/	1.60	1.47	4.23	4.39	4.48	7
(100)	6	6	6	22.4	31.5	28.5	1.45	1.44	4.42	4.60	4.59	8
(111)	8	8	8	77.6	42.0	71.5	1.37	1.30	4.76	4.83	4.94	9

^a Symmetry multiplicity of the growth form.

3.3 Adsorption at Cu(111) surface

3.3.1 Adsorption geometries and energies

Following a strategy similar to that used in previous works,^{53,54} both parallel and perpendicular adsorption orientations of the inhibitor on to Cu(111) surface have been considered. The geometries of inhibitor molecules adsorbed on the Cu(111) surface with a perpendicular (parallel) initial adsorption configuration were investigated and the most stable optimized structures are displayed in the upper (lower) panels of Fig. 5. To quantitatively appraise the interaction between each molecule and the copper surface, the adsorption energy (E_{ads}) was calculated using following formula

$$E_{\text{ads}} = E_{\text{mol/surf}} - (E_{\text{surf}} + E_{\text{mol}}) \quad (12)$$

where E_{mol} , E_{surf} , and $E_{\text{mol/surf}}$ are the total energies of isolated adsorbate, Cu(111) slab, and mol/Cu(111) system, respectively. Based on this definition, a negative value of E_{ads} corresponds to a stable adsorption structure. Calculated adsorption energies and structure parameters of inhibitor molecules adsorbed on the Cu(111) surface are summarized in Table 5.

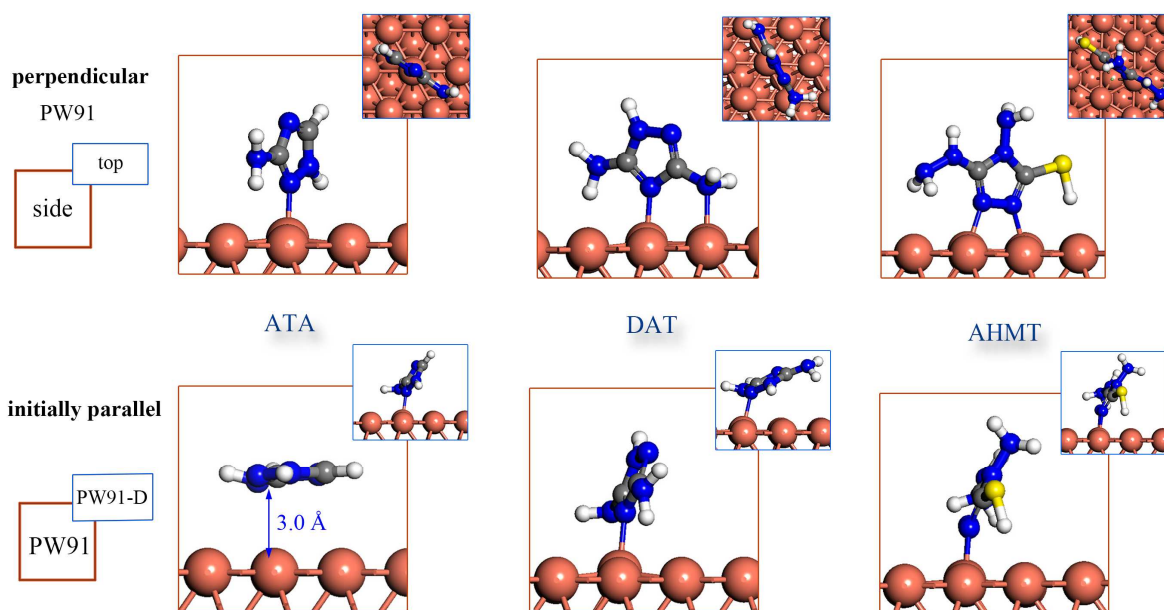


Fig. 5 Geometry optimized structures of ATA, DAT, and AHMT adsorbed on Cu(111). Only parts of the atoms of the slab model are shown for clarity.

Table 5 Structural parameters and adsorption energies of inhibitor molecules adsorbed on Cu(111) as obtained with the PW91 and PW91-D Functionals^a

Molecule@Cu(111)	perpendicular			initially parallel	
	Bond lengths (Å)	Δh_{Cu} ^b (Å)	E_{ads} (eV)	E_{ads} (eV)	θ^c (deg)
ATA	$R_{[\text{N}2-\text{Cu}]}$ 2.06 (2.05)	0.25 (0.21)	-0.67 (-0.84)	-0.26 (-0.76)	3.8 (59.9)
DAT	$R_{[\text{N}4-\text{Cu}]}$ 2.11 (2.10)	0.22 (0.21)	-0.76 (-0.99)	-0.61 (-0.94)	69.9 (27.2)
	$R_{[\text{N}7-\text{Cu}]}$ 2.22 (2.21)	0.12 (0.08)			
AHMT	$R_{[\text{N}1-\text{Cu}]}$ 2.01 (2.02)	0.06 (0.06)	-1.12 (-1.29)	-0.86 (-1.26)	64.2 (58.3)
	$R_{[\text{N}2-\text{Cu}]}$ 2.11 (2.09)	0.12 (0.10)			

^a Values in parentheses are those from PW91-D functional.

^b Δh_{Cu} denotes the distance that the copper has moved up.

^c The angle θ is defined by the two planes of molecular cyclic skeleton and the horizontal substrate.

For perpendicular adsorption modes, the PW91 and PW91-D functionals give almost identical structures (just give the structures of the former for simplicity), but discrepancies appear for initially parallel modes. These discrepancies can be seen in the lower panels of Fig. 5, where the PW91-D gives a more tilted adsorption configuration. Similar results were obtained by Kokalj *et al.*⁵³ in their study of the adsorption of dehydrogenated benzotriazole on perfect copper surfaces. ATA is a very special case since PW91 shows nearly parallel structure, and the molecule surface height of 3.0 Å (substantially equal to the sum of the van der Waals radii $r_{\text{vdw}}^{\text{N}} + r_{\text{vdw}}^{\text{Cu}} = 1.55 + 1.40 = 2.95 \text{ \AA}$)⁵⁵ indicates a physisorption nature. As for the adsorption energies, it can be seen that the perpendicular configuration is energetically more stable than the initially parallel configuration for all the three inhibitors. This confirms that azoles bond perpendicularly with σ -orbitals to transition metals with fully occupied

d-band (such as copper).⁵⁶ The non-perpendicular state appears to be either unstable or metastable, it is either a very shallow minimum or a flat plateau, and the molecules are steered directly into perpendicular (chemisorbed) state.

Analysis of the frozen perpendicular configurations reveals that inhibitors actually bond directly with Cu through nitrogen atoms. Concrete speaking, ATA molecule is adsorbed on top of a Cu atom with a single N2 atom; DAT molecule mainly adsorbs *via* N4 atom, as well as a relatively weak interaction *via* N7 atom; whereas AHMT is bonded through the bridge-N1, N2 atoms. These results indeed confirm above active site analysis. As evident from Table 5, the N–Cu bond lengths are in the range between 2.0–2.2 Å thus being comparable to the sum of N and Cu covalent radii ($r_{\text{cov}}^{\text{N}} + r_{\text{cov}}^{\text{Cu}} = 0.71 + 1.32 = 2.03$ Å), which be categorized as chemisorption. The three molecules interact strongly with the surface and the strength of the chemisorption increases in the order ATA < DAT < AHMT with the adsorption energies of –0.67, –0.76, and –1.12 eV, respectively. Due to the strong interaction, the adsorption induced corrugation, as measured by Δh_{Cu} (defined in Table 5), is about 0.06–0.25 Å. The PW91-D gives more exothermic adsorption energies than the PW91, although it may more appropriately capture the relative stability of different adsorption modes, we hold that under current circumstance the PW91 results should be more appropriate than the PW91-D results, because it is known that PW91 functional often overestimates the chemisorption energies.^{57,58} The absolute value of adsorption energy for ATA (*i.e.*, 0.67 eV) is slightly higher than the earlier reported PBE result (0.6 eV)^{33,55}, this can be considered acceptable, since PW91 gives slightly higher adsorption energy than PBE for molecule–metal(*hkl*) system (as reviewed by Hammer and Norskov)⁵⁹.

3.3.2 Projected density of states

Insights into the interaction between inhibitor molecule and Cu(111) surface can be obtained from the projected density of states (PDOS), as shown in Fig. 6 (*PW91 results*). A Gaussian broadening width of 0.04 eV has been applied. The Fermi level is set to zero, as shown by the vertical line.

Figure 6 shows the PDOS of the inhibitor/Cu(111) system before and after molecule–surface interaction: the upper panels presents the PDOS for the molecule located 7 Å above the Cu(111) surface, while the lower panels shows the PDOS for the molecule with the perpendicular adsorption mode. The upper panels can be used to highlight the high-lying molecular valence states before the interaction occurs.^{33,60,61} It is obvious that several molecular states lie at the position of the copper *d*-band, which can be considered to describe the molecule–surface bonding upon adsorption. When the inhibitor molecule adsorbs on the copper surface (shown in the lower

panels), the molecular peaks broadened slightly due to the hybridization between molecular and metal states. As a consequence, the distributions of density of states for both Cu and adsorbates are skewed toward the lower energy values. In the energy range from -4.5 to -1.5 eV, the molecular PDOS of AHMT is considerably less spiky compared to that of ATA/DAT, suggesting the stronger molecule–surface bond.

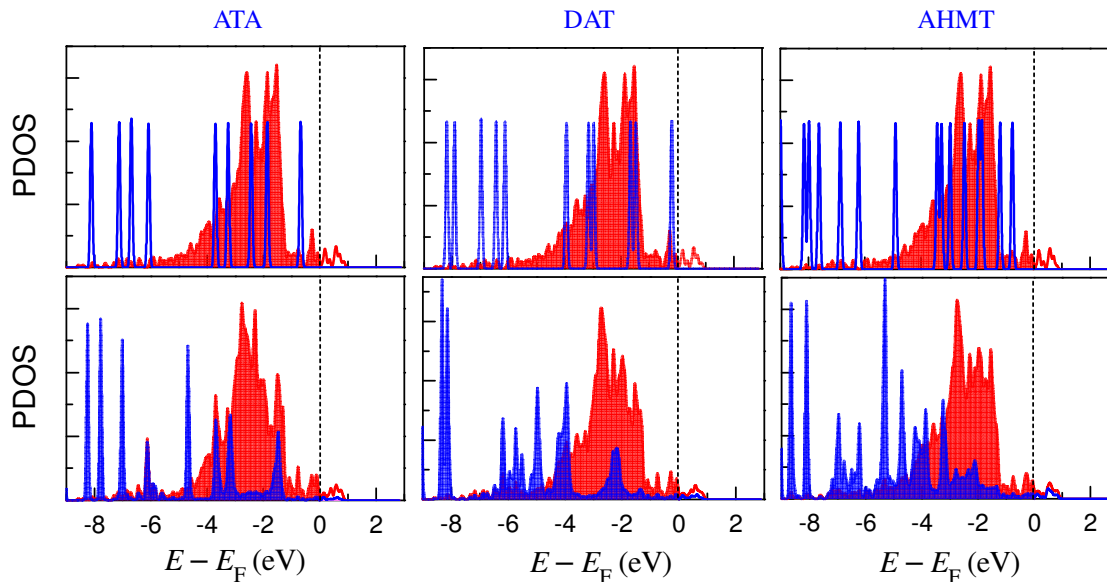


Fig. 6 Superimposed density of states for ATA, DAT, and AHMT projected to the molecule (blue) and to the Cu atoms that bond with the molecule (red).

(upper panels: inhibitor above Cu(111); lower panels: perpendicular adsorption configurations in Fig. 5)

3.3.3 Charge density difference

The corresponding rearrangement of electronic charge upon the adsorbed inhibitor molecules can be obtained by subtracting the charge densities of the non-interacting systems (isolated copper surface ρ_{surf} , and isolated of inhibitor molecule ρ_{mol} , both frozen at their final equilibrium configuration upon adsorption) from those where the inhibitors interact with the Cu(111) surface $\rho_{\text{mol/surf}}$:

$$\Delta\rho = \rho_{\text{mol/surf}} - (\rho_{\text{mol}} + \rho_{\text{surf}}) \quad (13)$$

The charge density difference of the most stable adsorption configuration for all three corrosion inhibitor molecules is shown in Fig. 7, this distinctly demonstrates the complex interplay between the different orbitals of metal and inhibitor molecule. The formation of direct N–Cu bonds can be seen by the charge redistribution between the corresponding N and Cu atoms, *i.e.*, the charge flows from these atoms toward the center of N–Cu bonds. This covalent interaction is not very strong, because the Cu has the *d*-band completely below the Fermi energy. There is persuasive evidence that for these neutral azole/metal adsorption systems, the contribution of

dipole interactions to the molecule–surface bonding is significant.^{50, 62} Besides, there is an accumulation of charge (red regions) located in between bottommost hydrogen atoms and the copper surface, suggesting the existence of the weak X–H...Cu hydrogen bond (X = N or S atom).⁶³ The adsorption between inhibitor molecules and copper surface can be strengthened through this type of bond.

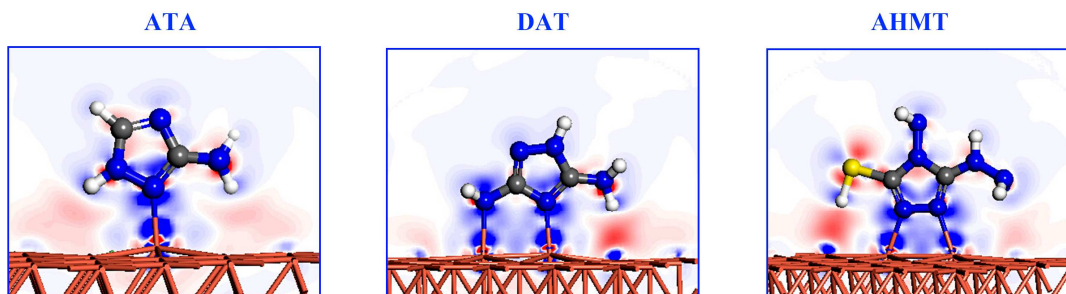


Fig. 7 Charge density difference of ATA, DAT, and AHMT molecules chemisorbed on Cu(111) surface with the perpendicular adsorption configurations (*PW91 results*).

(The value of the mapped field is drawn in linear scale from -0.06 to $+0.06 e \text{ \AA}^{-3}$, blue and red refer to an decrease and increase of the electronic density, respectively)

3.3.4 QTAIM analyses

In the QTAIM analyses, the existence of the interatomic interaction is indicated by the presence of a so-called bond critical point (BCP). The properties at the BCPs are analysed in terms of the following parameters: the electron density (ρ_{bcp}), its Laplacian (L_{bcp}), the electron energy density (H_{bcp}) and absolute ratio of kinetic and potential energies densities ($-G_{\text{bcp}}/V_{\text{bcp}}$). In their review Macchi and Sironi have summarized that the covalent bonds involving transition metals are characterized by: (i) the small values of ρ_{bcp} and L_{bcp} ; (ii) negative total energy density $H_{\text{bcp}} < 0$ (that is, in covalent bonds the potential energy is dominated over kinetic energy).⁶⁴ Espinosa *et al.* proposed use of the $-G_{\text{bcp}}/V_{\text{bcp}}$ ratio classify different types of interactions: if $-G_{\text{bcp}}/V_{\text{bcp}} > 1$ the interaction is non-covalent in nature; if $0.5 < -G_{\text{bcp}}/V_{\text{bcp}} < 1$, the interaction is partly covalent.⁶⁵

As shown in Fig. 8, the interactions between Cu and the active sites of three inhibitors can be confirmed by the existence of the BCP of the Cu...N contact. The corresponding topological parameters at the BCPs have been listed in Table 6. The electron density ρ_{bcp} can be used to characterize the relative strength of the Cu...N contact. As seen in Table 6, Cu...N7 exhibits weaker interactions compared with the other bonds, accompanied with a longer bond length. If considering multiple active adsorption sites, the relative order of the ρ_{bcp} for the three Cu–inhibitor complexes is: Cu–AHMT > Cu–DAT > Cu–ATA, which is consistent with the relative order of the inhibition efficiency. The positive values of L_{bcp} , $-G_{\text{bcp}}/V_{\text{bcp}} < 1$ and the nearly zero values of H_{bcp} suggest that the interactions between Cu and N atom of the inhibitors are predominated by the electrostatic interactions as well as

partial covalent characters in nature.

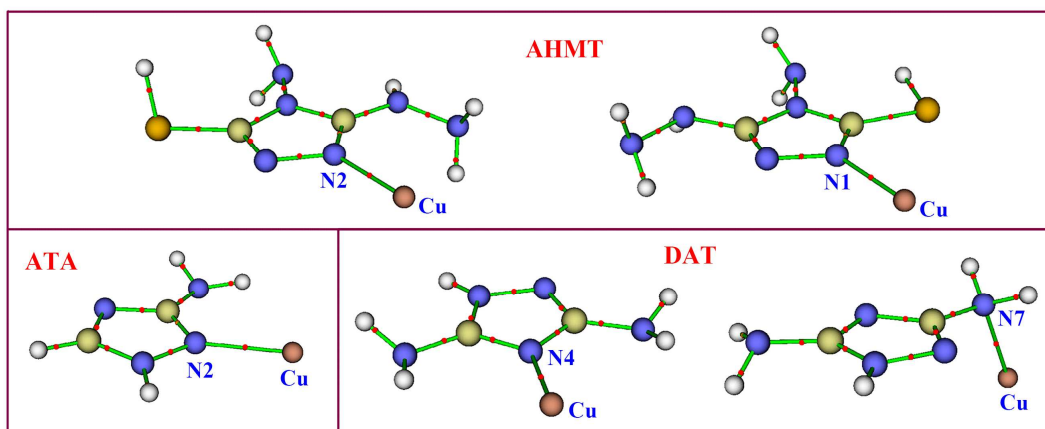


Fig. 8 The molecular graphs of the formed Cu–inhibitor complexes, where the BCPs are denoted as small red dots.

Table 6 Calculated topological parameters at the BCPs of the Cu...N contacts

Complexes	BCP	ρ_{bcp}	L_{bcp}	H_{bcp}	$-G_{\text{bcp}}/V_{\text{bcp}}$	$R_{\text{Cu}\cdots\text{X}}^a$
Cu–ATA	Cu...N2	0.0732	0.3315	–0.0121	0.8870	2.056
Cu–DAT	Cu...N4	0.0748	0.3288	–0.0129	0.8798	2.052
	Cu...N7	0.0551	0.1999	–0.0107	0.8501	2.206
Cu–AHMT	Cu...N1	0.0740	0.3371	–0.0123	0.8871	2.054
	Cu...N2	0.0745	0.3372	–0.0125	0.8856	2.052

^a $R_{\text{Cu}\cdots\text{X}}$: acceptor–donor distance in Å.

3.4 Diffusion of corrosive particle in the inhibitor membrane

The calculated densities of the inhibitor membranes are shown in Fig. 9. It is clear from Fig. 9 that three inhibitor membranes ATA, DAT, and AHMT reach equilibrium after 80 ps MD simulation. In order to obtain the accurate average density, the values from 80 ps to 300 ps are adopted. The calculated densities of three inhibitors ATA, DAT, and AHMT are 1.31, 1.49, and 1.54 g cm^{–3}, respectively. Self-diffusion coefficient (D) of the molecule is the best measurement of the diffusion behavior. It can be used to describe the migration rate of a corrosive species in inhibitor membranes. Normally, D is calculated from the mean square displacement (MSD) by the Einstein diffusion equation⁶⁶:

$$\text{MSD} = \left\langle [R_i(t) - R_i(0)]^2 \right\rangle \quad (14)$$

$$D = \frac{1}{6N_a} \lim_{t \rightarrow \infty} \frac{d}{dt} \sum_{i=1}^{N_a} \left\langle [R_i(t) - R_i(0)]^2 \right\rangle \quad (15)$$

where N_a is the number of diffusive atoms; $R_i(t)$ and $R_i(0)$ are positions of corrosive species at time t and 0, respectively. The limiting slope of MSD as a function of time can be used to evaluate the diffusion coefficient of a molecule undergoing random Brownian motion in the three dimensions. Fig. 10 depicts the MSD diagrams of H_3O^+ in the inhibitor membranes. As illustrated in Fig. 10, the MSD diagram showed a smooth increase during the initial simulation process; the anomalous diffusion⁶⁷ took place between 650 ps and 1000 ps. Then the effective diffusion coefficients of H_3O^+ calculated from the MSD slopes over 300–650 ps by means of Eq. (15) are listed in Table 7. As previously reported by Zhang and co-workers,⁶⁸ the diffusion coefficient of H_3O^+ in water without any inhibitors is $0.831 \times 10^{-5} \text{ cm}^2 \text{ s}^{-1}$. The diffusion coefficients of H_3O^+ in the inhibitor membranes sharply decrease comparing with those in water. This indicates that these inhibitor membranes could efficiently restrain the migration of corrosive particle.

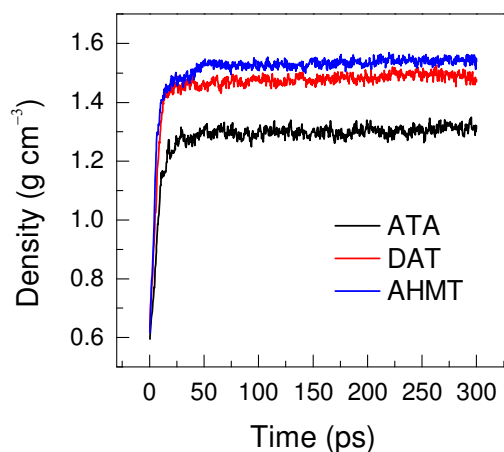


Fig. 9 Calculated densities of inhibitor membranes ATA, DAT and AHMT.

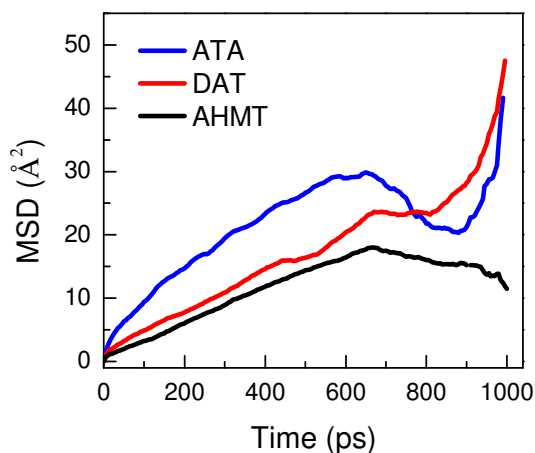


Fig. 10 MSD plot of H_3O^+ in the inhibitor membranes at 303 K during 1 ns MD simulation.

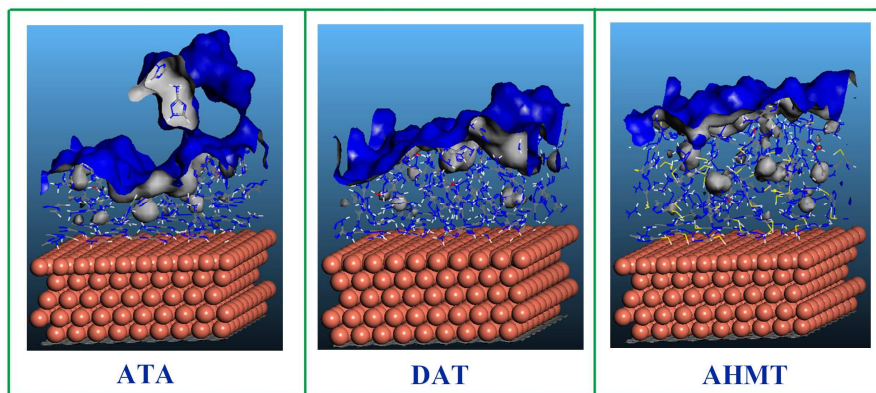
Table 7 Calculated diffusion coefficients (D) and fractional free volume (ζ) values

Membrane	D ($\times 10^{-7}$ cm ² s ⁻¹)	ζ
ATA	2.154	0.21
DAT	1.456	0.14
AHMT	1.275	0.069

Furthermore, to evaluate free volume inside each inhibitor membrane, fractional free volume (ζ) is defined as follow:

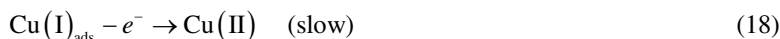
$$\zeta = \frac{V_f}{V_f + V_0} \quad (16)$$

where V_f is the free volume, and V_0 is the volume occupied by the corrosion inhibitors in the membrane. H_3O^+ was selected as probe particle (connolly radius = 1.35 Å) in the system. It is generally recognized that a large ζ means there are abundant cavities among the inhibition membrane, and the migration probability of corrosive particle is high, which induces to large diffusion coefficient and low inhibition efficiency.⁶⁹ On the one hand, a small ζ infers to small diffusion coefficient and high inhibition efficiency. In this work, the last frame was extracted after 300 ps MD simulation and the fractional free volume analysis was performed. The free volume distributions of three inhibitor membranes are shown in Fig. 11. The present ζ values (see Table 7) in three inhibitor membranes are in the order $\zeta(\text{AHMT}) < \zeta(\text{DAT}) < \zeta(\text{ATA})$. This indicates that the size of cavity which is accessible for the corrosive particle decreases in the order $\text{ATA} > \text{DAT} > \text{AHMT}$. It agreed well with the result of the calculated diffusion coefficient. The diffusion model results showed that it is reasonable and practical to evaluate the inhibition performance, at least qualitatively.

**Fig. 11** Free volume distributions of three inhibitor membranes probed by H_3O^+ .

3.5 Mechanism of adsorption and inhibition

Now, after discussing the inhibition mechanism at molecular/atomic level, clarifying the actual reaction process is necessary. According to the potential-pH diagram shown in Fig. S in the supporting information, the protective Cu₂O and CuO oxide films can be easily dissolved at low pH values. As shown in Fig. 12, the dissolution of copper in HNO₃ proceeded according to the following steps:



where Cu(I)_{ads} is an adsorbed species at the copper surface and does not diffuse into the bulk solution. The cathode reduction of oxygen can be expressed as follow:



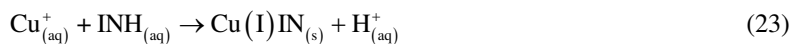
Besides, the nitrate ions are readily reduced:



According to the literatures,^{70, 71} two mechanisms have been proposed to explain the high inhibiting efficiency recorded for the inhibitors of interest, designated as INH. One mechanism attributes the phenomenon to the formation of an adsorbed layer of INH, *i.e.*,



where Cu: INH_(ads) refers to INH adsorbed on the copper surface. The other mechanism postulates a protective Cu(I)IN film on the surface, which inhibits the anodic dissolution reaction, *i.e.*,



The Cu(I)IN complex is favored at more anodic potentials in less acidic media; however, the adsorbed species is formed in more acidic media under cathodic potentials.

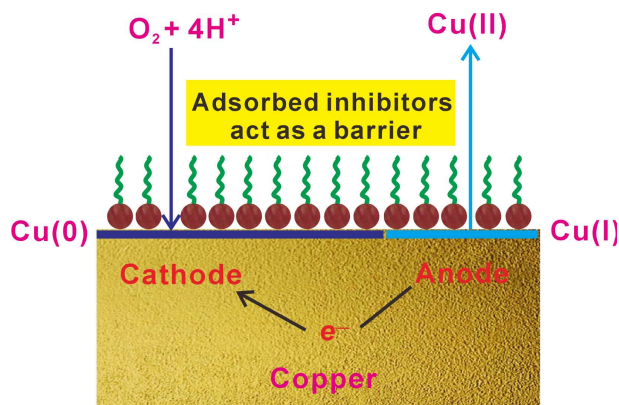


Fig. 12 Proposed scheme for the adsorption of inhibitors on the copper surface in acid medium.

4 Conclusions

In the present study, the interactions between three triazole derivatives and copper has been systematically investigated by density functional theory in combination with the QTAIM theory and molecular dynamics. The main conclusions are summarized as follows:

- (i) Quantum chemical calculation results reveal that the inhibitor molecules have strong adsorption sites by which they can directly adsorb onto copper surface *via* sharing of electrons with copper atoms.
- (ii) The energies of the σ -molecular orbitals were decisive for the adsorption performance.
- (iii) The inhibitors can chemisorb onto Cu(111) with the molecular plane being nearly perpendicular to the surface.
- (iv) The agreement of the diffusion model results with the trend of inhibition efficiency (*IE*) indicates that the pertinent effect (the restraintment of migration of corrosive species through the inhibitor membrane) is a factor that contributes to *IE* of inhibitors.

Acknowledgements

This research was sponsored by the National Natural Science Foundation of China (21376282). The authors would like to thank Dong Yang for his valuable discussions. We also thank the anonymous referees for valuable criticisms and useful suggestions that helped us to improve the quality of our present and future work.

References

- 1 B. V. Appa Rao, M. Y. Iqbal and B. Sreedhar, *Electrochim. Acta*, 2010, **55**, 620-631.
- 2 S. John and A. Joseph, *RSC Adv.*, 2012, **2**, 9944-9951.
- 3 S. Banerjee, A. Mishra, M. M. Singh, B. Maiti, B. Ray and P. Maiti, *RSC Adv.*, 2011, **1**, 199-210.
- 4 M. L. Zheludkevich, K. A. Yasakau, S. K. Poznyak and M. G. S. Ferreira, *Corros. Sci.*, 2005, **47**, 3368-3383.

- 5 M. K. Awad, M. R. Mustafa and M. M. A. Elnga, *J. Mol. Struct. Theochem*, 2010, **959**, 66-74.
- 6 A. Kosari, M. H. Moayed, A. Davoodi, R. Parvizi, M. Momeni, H. Eshghi and H. Moradi, *Corros. Sci.*, 2014, **78**, 138-150.
- 7 P. Roy, A. Pal and D. Sukul, *RSC Adv.*, 2014, **4**, 10607-10613.
- 8 A. Zarrouk, B. Hammouti, H. Zarrok, M. Bouachrine, K. F. Khaled and S. S. Al-Deyab, *Int. J. Electrochem. Sci.*, 2012, **7**, 89-105.
- 9 A. Zarrouk, B. Hammouti, S. S. Al-Deyab, R. Salghi, H. Zarrok, C. Jama and F. Bentiss, *Int. J. Electrochem. Sci.*, 2012, **7**, 5997-6011.
- 10 A. Zarrouk, B. Hammouti, A. Dafali and F. Bentiss, *Ind. Eng. Chem, Res.*, 2013, **52**, 2560-2568.
- 11 J. Zhang, W. Yu, L. Yu, Y. Yan, G. Qiao, S. Hu and Y. Ti, *Corros. Sci.*, 2011, **53**, 1331-1336.
- 12 J. Radilla, G. E. Negrón-Silva, M. Palomar-Pardavé, M. Romero-Romo and M. Galván, *Electrochim. Acta*, 2013, **112**, 577-586.
- 13 S. Q. Hu, A. L. Guo, Y. F. Geng, X. L. Jia, S. Q. Sun and J. Zhang, *Mater. Chem. Phys.*, 2012, **134**, 54-60.
- 14 V. Jaiswal, R. B. Rastogi, J. L. Maurya, P. Singh and A. K. Tewari, *RSC Adv.*, 2014, **4**, 13438-13445.
- 15 A. Kokalj, *Acta Chim. Slov.*, 2014, **61**, 340-349.
- 16 Harihara.Pc and J. A. Pople, *Theor. Chim. Acta*, 1973, **28**, 213-222.
- 17 G. Klopman, *J. Am. Chem. Soc.*, 1968, **90**, 223-234.
- 18 L. Yang and Y. Dong, *Carbohydr. Res.*, 2011, **346**, 2457-2462.
- 19 B. Delley, *J. Chem. Phys.*, 2000, **113**, 7756-7764.
- 20 J. P. Perdew, K. Burke and M. Ernzerhof, *Phys. Rev. Lett.*, 1996, **77**, 3865-3868.
- 21 J. P. Perdew, K. Burke and Y. Wang, *Phys. Rev. B*, 1996, **54**, 16533-16539.
- 22 W. Wang, Z. Li, Q. Sun, A. Du, Y. Li, J. Wang, S. Bi and P. Li, *Corros. Sci.*, 2012, **61**, 101-110.
- 23 E. E. Oguzie, Y. Li, S. G. Wang and F. Wang, *RSC Adv.*, 2011, **1**, 866-873.
- 24 S. H. Chen, S. Q. Sun, B. J. Lian, Y. F. Ma, Y. G. Yan and S. Q. Hu, *Surf. Sci.*, 2014, **620**, 51-58.
- 25 F. Ortman, F. Bechstedt and W. Schmidt, *Phys. Rev. B*, 2006, **73**, 205101.
- 26 R. F. W. Bader, *Atoms in Molecules: A Quantum Theory*, Oxford University Press, New York, 1994.
- 27 T. Lu and F. W. Chen, *J. Comput. Chem.*, 2012, **33**, 580-592.
- 28 H. J. C. Berendsen, J. P. M. Postma, W. F. Vangunsteren, A. Dinola and J. R. Haak, *J. Chem. Phys.*, 1984, **81**, 3684-3690.
- 29 H. Sun, *J. Phys. Chem. B*, 1998, **102**, 7338-7364.
- 30 R. G. Pearson, *Inorg. Chem.*, 1988, **27**, 734-740.
- 31 V. S. Sastri and J. R. Perumareddi, *Corrosion*, 1997, **53**, 617-622.
- 32 R. Parthasarathi, J. Padmanabhan, V. Subramanian, B. Maiti and P. K. Chattaraj, *J. Phys. Chem. A*, 2003, **107**, 10346-10352.
- 33 A. Kokalj and S. Peljhan, *Langmuir*, 2010, **26**, 14582-14593.
- 34 N. Kovačević and A. Kokalj, *Corros. Sci.*, 2011, **53**, 909-921.
- 35 A. Kokalj, *Electrochim. Acta*, 2010, **56**, 745-755.
- 36 Y. Yan, W. H. Li, L. K. Cai and B. R. Hou, *Electrochim. Acta*, 2008, **53**, 5953-5960.
- 37 Y. Jiang and J. B. Adams, *Surf. Sci.*, 2003, **529**, 428-442.
- 38 Y. G. Avdeev and Y. I. Kuznetsov, *Russ. Chem. Rev.*, 2012, **81**, 1133-1145.
- 39 G. Gece, *Corros. Sci.*, 2008, **50**, 2981-2992.
- 40 N. Khalil, *Electrochim. Acta*, 2003, **48**, 2635-2640.
- 41 M. Lebrini, F. Bentiss, H. Vezin and M. Lagrenee, *Appl. Surf. Sci.*, 2005, **252**, 950-958.
- 42 S. G. Zhang, W. Lei, M. Z. Xia and F. Y. Wang, *J. Mol. Struct. Theochem*, 2005, **732**, 173-182.
- 43 H. M. Abd El-Lateef, V. M. Abbasov, L. I. Aliyeva, E. E. Qasimov and I. T. Ismayilov, *Mater. Chem. Phys.*, 2013, **142**,

- 502-512.
- 44 R. R. Contreras, P. Fuentealba, M. Galvan and P. Perez, *Chem. Phys. Lett.*, 1999, **304**, 405-413.
- 45 C. Morell, A. Grand and A. Toro-Labbe, *J. Phys. Chem. A*, 2005, **109**, 205-212.
- 46 F. L. Hirshfeld, *Theor. Chim. Acta*, 1977, **44**, 129-138.
- 47 A. Arya and E. A. Carter, *Surf. Sci.*, 2004, **560**, 103-120.
- 48 N. Lang and W. Kohn, *Phys. Rev. B*, 1971, **3**, 1215-1223.
- 49 M. P. J. Punkkinen, Q. M. Hu, S. K. Kwon, B. Johansson, J. Kollar and L. Vitos, *Philos. Mag.*, 2011, **91**, 3627-3640.
- 50 S. Peljhan and A. Kokalj, *Phys. Chem. Chem. Phys.*, 2011, **13**, 20408-20417.
- 51 H. L. Skriver and N. M. Rosengaard, *Phys. Rev. B*, 1992, **46**, 7157-7168.
- 52 J. Radilla, M. Boronat, A. Corma and F. Illas, *Phys. Chem. Chem. Phys.*, 2010, **12**, 6492-6498.
- 53 S. Peljhan, J. Koller and A. Kokalj, *J. Phys. Chem. C*, 2014, **118**, 933-943.
- 54 N. Kovacevic and A. Kokalj, *Corros. Sci.*, 2013, **73**, 7-17.
- 55 A. Kokalj, S. Peljhan, M. Finsgar and I. Milosev, *J. Am. Chem. Soc.*, 2010, **132**, 16657-16668.
- 56 N. Kovacevic and A. Kokalj, *Mater. Chem. Phys.*, 2012, **137**, 331-339.
- 57 S. J. Jenkins, *Surf. Sci.*, 2006, **600**, 1431-1438.
- 58 V. V. Mihaleva, R. A. van Santen and A. P. J. Jansen, *J. Phys. Chem. B*, 2001, **105**, 6874-6879.
- 59 B. Hammer and J. K. Nørskov, *Adv. Catal.*, 2000, **45**, 71-129.
- 60 S. Sun, Y. Geng, L. Tian, S. Chen, Y. Yan and S. Hu, *Corros. Sci.*, 2012, **63**, 140-147.
- 61 M. Finsgar, A. Lesar, A. Kokalj and I. Milosev, *Electrochim. Acta*, 2008, **53**, 8287-8297.
- 62 A. Kokalj, *Phys. Rev. B*, 2011, **84**, 045418.
- 63 R. H. Crabtree, O. Eisenstein, G. Sini and E. Peris, *J. Organomet. Chem.*, 1998, **567**, 7-11.
- 64 P. Macchi and A. Sironi, *Coord. Chem. Rev.*, 2003, **238**, 383-412.
- 65 E. Espinosa, I. Alkorta, J. Elguero and E. Molins, *J. Chem. Phys.*, 2002, **117**, 5529-5542.
- 66 X. Michalet, *Phys. Rev. E*, 2010, **82**, 059904
- 67 F. Mullerplathe, S. C. Rogers and W. F. Vangunsteren, *Chem. Phys. Lett.*, 1992, **199**, 237-243.
- 68 L. F. Liu, J. X. Liu, J. Zhang, L. You, L. J. Yu and G. M. Qiao, *Chem. J. Chin. Univ.*, 2010, **31**, 537-541.
- 69 A. L. Guo, G. C. Duan, K. He, B. Sun, C. C. Fan and S. Q. Hu, *Comput. Theor. Chem.*, 2013, **1015**, 21-26.
- 70 M. M. Antonijevic and M. B. Petrovic, *Int. J. Electrochem. Sci.*, 2008, **3**, 1-28.
- 71 K. F. Khaled and M. A. Amin, *Corros. Sci.*, 2009, **51**, 2098-2106.